Chemical Science

ROYAL SOCIETY OF CHEMISTRY

EDGE ARTICLE

View Article Online
View Journal | View Issue

Cite this: *Chem. Sci.*, 2025, **16**, 18821

All publication charges for this article have been paid for by the Royal Society of Chemistry

Axial fluorine coordination boosts the activity and durability of Fe single-atom catalysts in room-temperature Na–S batteries

Xue Zhong, Yujie Huang, Jieming Cai, Dongyang Cai, Zidong He, Zhenglei Geng, Wentao Deng, Guoqiang Zou, Hongshuai Hou * and Xiaobo Ji

Received 7th August 2025
Accepted 4th September 2025

DOI: 10.1039/d5sc05972k

rsc.li/chemical-science

Single-atom catalysts (SACs) hold promise for addressing challenges of polysulfide shuttle and sluggish sulfur reduction reaction (SRR) in room-temperature (RT) Na–S batteries. However, their structural durability under harsh electrochemical conditions remains a critical concern. Herein, we propose an effective strategy to optimize and stabilize the active sites of Fe single atoms (Fe_{SACS}) by modulating the local geometries through axial fluorine (F) coordination, thus significantly alleviating the stability problems faced by conventional high-performance but deactivation-prone Fe–N–C catalysts. Density functional theory (DFT) calculations and experimental results confirm that the enhanced Fe–F interactions in the second shell layer play a key role in maintaining the structural integrity of the single atoms during synthesis and operation and effectively inhibit the agglomeration behavior of Fe atoms. The F axial coordination with the optimized electronic structure enhanced the d–p hybridization between the Fe 3d orbitals and the sulfur intermediates, which significantly promoted the SRR kinetics and catalytic durability. Through comprehensive spectroscopic investigations, we further elucidate that the sulfur species undergo quasi-solid–solid conversion pathways on Fe_{SACS}-FCNT@S electrodes, effectively suppressing polysulfide dissolution. This work establishes a universal paradigm for designing durable SAC systems through rational coordination engineering while providing fundamental insights into structure–stability relationships for advanced metal–sulfur batteries.

Introduction

Lithium-ion batteries (LIBs) have long been a core energy storage technology underpinning modern sustainable energy systems, but further large-scale application of LIBs is increasingly limited due to the high cost of lithium resources and limited scope for performance improvement.[1–3] In this technological context, the RT Na–S battery system based on multi-electron transfer chemistry has become one of the most competitive candidates for large-scale grid energy storage due to its high theoretical specific capacity (1675 mA h g^{-1}), abundant resources and low costs of Na and S.[4,5] However, the high solubility of sodium polysulfides (NaPSs) during operation and the resulting shuttle effect, as well as severe slow reaction kinetics of the sulfur cathode, can trigger severe capacity degradation and limit cycle life. Addressing these challenges requires innovative strategies in catalyst design to regulate the complex sulfur phase transition and achieve the efficient kinetics required.[6–9]

d-Block single-atom catalysts, characterized by atomically dispersed metal sites that maximize active interface exposure, have emerged as a transformative paradigm for regulating NaPS conversion kinetics.[10–12] The well-defined site structures and the coordination environments of isolated metal sites are easier to regulate than those of metal nanoparticles and nanoclusters, which provide an atomic-scale operating space for precise modulation of their catalytic activities.[13–15] Among various coordination architectures, planar tetracoordinated $M–N_4$ moieties have been identified as effective catalytic centers for NaPS transformation.[16,17] Nevertheless, the inherent symmetry of these configurations induces anisotropic adsorption behavior toward intermediates, fundamentally constraining the optimization of the geometric and electronic structures of active sites.[18–21] In stark contrast, second-shell axial engineering—achieved through heteroatom incorporation (O/S/P/Cl)—leverages long-range d–p orbital coupling to induce directional charge transfer.[22–25] The resultant electron density gradient not only amplifies localized polarized electric fields but also strategically modulates d-band center positions, thereby synergistically enhancing sulfur species adsorption and subsequent transformation dynamics.[16,26–28]

While substantial progress has been made in deciphering the structure–activity relationships of SACS for RT Na–S batteries, the critical challenge of sustaining atomic dispersion under operational conditions remains underexplored—

College of Chemistry and Chemical Engineering, Central South University, Changsha, 410083, P. R. China. E-mail: hs-hou@csu.edu.cn

a prerequisite for practical implementation.[29–31] It is well-established that the irreversible leaching of SACs into clusters/nanoparticles during prolonged cycling fundamentally compromises their durability.[32,33] Current research predominantly focuses on optimizing intrinsic activity through coordination engineering, yet crucially overlooks the dynamic stability of metal centers during continuous sulfur redox events. Extended reaction durations inevitably exacerbate atomic aggregation, accelerating catalyst deactivation. This underscores the imperative to engineer[34,35] both the thermodynamic stability of isolated sites and kinetic resistance to reconstruction—a dual stabilization paradigm intrinsically linked to the macroscopic performance of SACs.

Herein, we present a fluorine-mediated axial coordination strategy to precisely regulate the spatial configuration and local electronic structure of Fe single-atom sites (FeN_4) anchored on a carbon matrix. Systematic DFT calculations coupled with experimental validation reveal that fluorine coordination induces the 3d orbital reconfiguration of Fe centers and strengthens d–p hybridization with sulfur species, thereby significantly enhancing the intrinsic SRR kinetics. Remarkably, the optimized Fe_{SACS}-FCNT@S demonstrates exceptional structural robustness, retaining atomic dispersion even after 150 cycles at 0.2 A g^{-1} while delivering a high capacity retention of 589.5 mA h g^{-1}. Combining various characterization studies such as *operando* sulfur K-edge XAS, TOF-SIMS and *ex situ* XPS, we reveal that Fe_{SACS}-FCNT@S is capable of inducing a quasi-solid sulfur conversion pathway, effectively inhibiting the generation and diffusion of soluble NaPSs. This work provides mechanistic insights into the design of atomically dispersed catalysts for RT Na–S battery systems and emphasizes the critical role of axial ligand engineering in achieving efficient sulfur conversion and long-term stability.

Results and discussion

In order to elucidate the nature of the kinetic behavior of the FeN_4–F active site-catalyzed SRR and its interaction mechanism with the reaction intermediates, DFT simulations were carried out from the intrinsic properties of the electronic structure of the 3d orbitals of Fe atoms. First, the structural models of FeN_4–F and FeN_4 were constructed and optimized, and the adsorption behaviors of the sulfur intermediates were investigated on the basis of the optimized substrate configurations. In RT Na–S batteries, d–p orbital hybridization is widely recognized as a critical descriptor of catalytic activity.[36,37] Projected density of states (PDOS) analysis revealed distinct orbital features before and after F coordination (Fig. 1a).[38]

For the FeN_4 site, the $d_{x^2-y^2}$ orbitals hybridized with four N ligands formed deeply occupied states and high-energy empty states, while the d_{z^2} orbital exhibited two localized bands. Upon F coordination, the d_{z^2} bands became delocalized due to strong Fe–F electronic coupling, with empty states near the Fermi level shifting to higher energies. Additionally, the degenerate d_{yz}/d_{xz} orbitals showed elevated energy levels under axial F perturbation. Collectively, axial F coordination induced an upward shift of the Fe 3d orbitals, resulting in a higher d-band center. Such

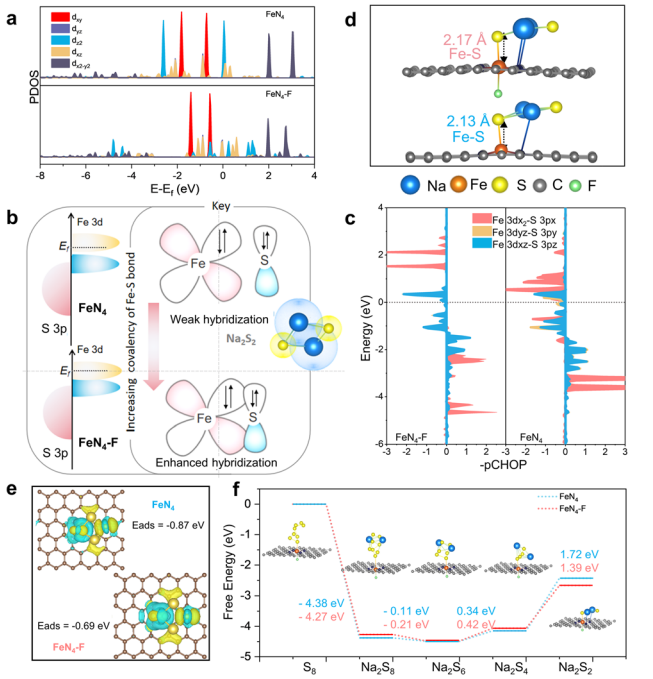

Fig. 1 Electronic structural analysis and orbital interactions from DFT calculations. (a) The PDOS of FeN_4 and FeN_4–F models. (b) Schematic diagram of the modulation of the d–p orbital hybridization. (c) –pCOHP analysis of the Fe–S bond after Na_2S_2 adsorption. (d) Electronic structure of Na_2S_2 after adsorption of FeN_4(up) and FeN_4–F(down). (e) Electron density differences of Na_2S_2 on FeN_4 and FeN_4–F. (f) Free energy diagrams of the sulfur reduction reaction on the surface of FeN_4 and FeN_4–F (the insets show the corresponding adsorption configurations).

electronic restructuring enhances the electron density within the d-band of the FeN_4–F model, promoting orbital overlap with sulfur intermediates and optimizing the adsorption–desorption equilibrium of reactive species, thereby accelerating SRR kinetics (Fig. 1b). To further elucidate the orbital hybridization mechanism between FeN_4 sites and sulfur species, we performed crystal orbital Hamiltonian population (–pCOHP) and PDOS analyses (Fig. 1c and S1) to quantify the modulation of Fe 3d–S 3p orbital coupling by F coordination.[39] The results demonstrate that F doping effectively modulates the coordination environment of FeN_4. This electronic restructuring is critical for catalyzing S–S bond cleavage. The elevated Fe 3d orbital energy levels enhance the coupling with the antibonding orbitals of polysulfides, thereby populating and weakening the S–S bonds.[40,41] Simultaneously, the strengthened d–p hybridization facilitates electron transfer from the Fe site to the adsorbed intermediates, dynamically promoting S–S bond rupture during reduction.[42] These synergistic effects significantly enhance the material's capacity to adsorb and convert polysulfide intermediates. Furthermore, by comparing the –pCOHP curves of FeN_4 with those of FeN_4–F systems, it was found that the σ* and σ bonding/anti-bonding orbitals exhibited a more pronounced energy level splitting between them upon the introduction of the F axial ligand. Notably, the σ* orbitals below the Fermi energy level are almost unoccupied in the FeN_4–F system, resulting in a more negatively skewed

overall –pCOHP value, suggesting that stronger and more stable metal–sulfur valence bonds are formed in this configuration. Fig. 1d depicts the geometrical configurations of Na_2S_2 molecules adsorbed on the FeN_4 and FeN_4–F models, respectively. It is noteworthy that the Fe–S bond lengths of the two models are only slightly different. In such cases, the nature of the orbital interaction becomes a more decisive factor than the absolute bond length in determining binding strength. –pCOHP analysis reveals that the FeN_4–F model displays significantly stronger metal–ligand orbital interactions, which contribute to enhanced structural stability. This finding highlights the pivotal role of axial F coordination in modulating the electronic coupling between the Fe center and sulfur species. In addition, charge density difference analysis further revealed the charge transfer behavior during the adsorption process (Fig. 1e): in the FeN_4–F system, the electron density of the Fe site was significantly reduced, while a significant electron accumulation was observed around the neighboring S atoms, suggesting that an effective charge transfer from the Na_2S_2 to the Fe site occurred. This charge rearrangement reinforces the stability of the adsorbed configuration. We further analyzed the Gibbs free energy changes of each intermediate state in the reduction pathway of S_8 to Na_2S_2. As shown in Fig. 1f, the conversion of Na_2S_4 to Na_2S_2 is accompanied by a significant energy barrier, suggesting that this step is the rate-determining step for the complete SRR. Notably, the energy barrier for this step in the FeN_4–F system is 1.39 eV, which is significantly lower than that of 1.72 eV in the FeN_4 model, suggesting that the F-ligand modulation effectively reduces the reaction energy barrier and provides a more favorable thermodynamic pathway to facilitate the final reduction of sulfur species. The above results demonstrate the positive modulation effect of F axial coordination engineering on catalyzing the conversion of sulfur species.

Guided by DFT computational insights, the axial F-coordinated FeN_4 active sites demonstrate enhanced catalytic potential for accelerating SRR kinetics. To experimentally validate this design, we developed a fluorine-doped carbon tube (FCNT) architecture through a templated synthesis strategy. As illustrated in Fig. 2a, MnO_2 nanorods served as sacrificial templates for the co-condensation of phenolic resin with fluorine-doped carbon dots (FCDs),[43] followed by pyrolysis at 700 °C under an argon atmosphere to yield FCNTs. A control sample (CNT) was synthesized under identical conditions without FCD addition to elucidate the role of fluorine modulation. Transmission electron microscopy (TEM) images show that both are tube-like structures (Fig. S2 and S3) and energy dispersive X-ray (EDS) elemental mapping analyses show the corresponding F signals (Fig. S3), which prove the successful doping of F. Subsequently, the $FeCl_3$–phenanthroline complex was anchored onto the CNT or FCNT substrate *via* a facile wet impregnation method, followed by thermal treatment to remove surface ligands, yielding the Fe_{SACS}-CNT and Fe_{SACS}-FCNT catalysts. TEM imaging combined with EDS elemental mapping confirmed the structural integrity of the carbon tubes after metal incorporation, with detectable Fe signals but no observable metallic nanoparticles (Fig. S4 and S5).

X-ray diffraction (XRD) patterns further revealed the absence of crystalline Fe phases in both Fe_{SACS}-FCNT and Fe_{SACS}-CNT catalysts, suggesting the possible presence of atomic dispersion of Fe species (Fig. 2b). However, in comparison to the two blank carbon-based controls without Fe incorporation (CNT and FCNT), a slight difference was observed, which manifested specifically as a narrowing of the diffraction peak around 20° (Fig. S6) indicative of enhanced graphitization degree of the carbon material following the secondary calcination process.[44] Atomic-resolution aberration-corrected high-angle annular dark-field scanning transmission electron microscopy (AC-HAADF-STEM) imaging provided direct evidence of the highly dispersed Fe species in Fe_{SACS}-FCNT, where numerous isolated bright spots—assigned to individual Fe atoms—are uniformly distributed across the carbon matrix (Fig. 2c and d) (encircled

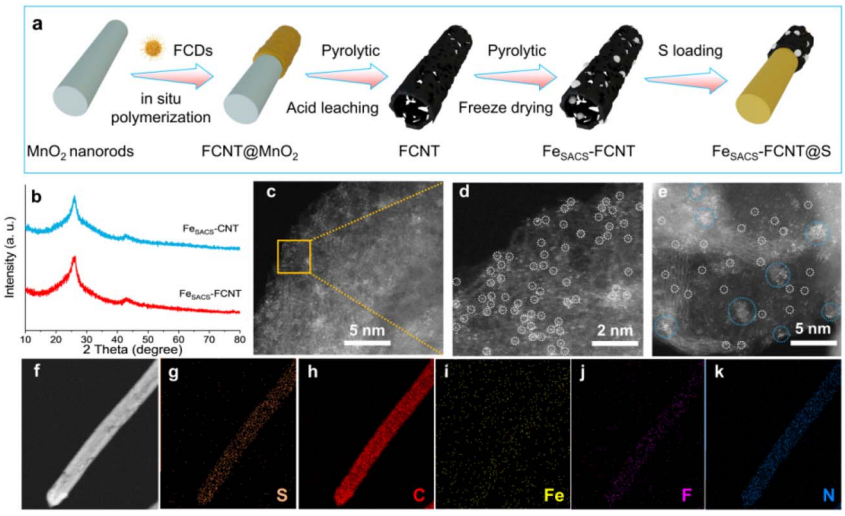

Fig. 2 (a) Schematic illustration of the synthetic procedure of Fe_{SACS}-FCNT@S. (b) XRD patterns of Fe_{SACS}-CNT and Fe_{SACS}-FCNT. HAADF-STEM images of (c and d) Fe_{SACS}-FCNT and (e) Fe_{SACS}-CNT. STEM image (f) and (g–k) elemental mapping images of Fe_{SACS}-FCNT@S.

by white dashed circles). In contrast, the reference Fe_{SACS}-CNT sample not only exhibited discrete single-atom-like features but also showed Fe clusters (encircled by blue dashed circles), indicating partial aggregation (Fig. 2e). These observations suggest that F axial modification strengthens the covalent interaction between the metal site and the support, thereby stabilizing the isolated Fe centers and suppressing cluster formation. This highlights the critical role of F doping in enhancing the structural stability of Fe_{SACS} during synthesis. Inductively coupled plasma optical emission spectroscopy (ICP-OES) analysis further confirmed nearly identical Fe loadings in both Fe_{SACS}-FCNT and Fe_{SACS}-CNT (1.15 wt% and 1.13 wt%, Table S1), ruling out any loading-dependent differences in catalytic performance. The as-synthesized catalysts and the two control carbon tube samples were further loaded with sulfur to fabricate a cathode for RT Na–S batteries. TEM images reveal that all four sulfur-loaded samples still retained the carbon tube shape (Fig. S7–S10). Sulfur is uniformly distributed both on the surface and within the interior of the tubes, which can be attributed to the hollow structure that facilitates efficient S_8 encapsulation. This structural feature also helps accommodate volumetric expansion during cycling, thereby mitigating structural degradation.

The corresponding EDS (Fig. 2f–k and S7–S10) results confirm the presence of sulfur signals, and XRD patterns (Fig. S11) exhibit characteristic diffraction peaks of orthorhombic sulfur,[11,45] further confirming successful sulfur incorporation. BET surface area and pore size distribution analyses show that Fe_{SACS}-FCNT and Fe_{SACS}-CNT possess high surface areas and well-defined mesoporous structures before sulfur loading. However, after sulfur infiltration, a significant decrease in surface area and near disappearance of mesopores are observed (Fig. S12), indicating effective penetration of sulfur into the porous framework—further evidence that S_8 has been successfully confined within the carbon tubes.[46,47] Moreover, Raman spectroscopy reveals comparable D-band and G-band intensities among all four sulfur-loaded samples (Fig. S13),[48,49] suggesting similar graphitization degrees and indicating that the introduction of single-atom Fe has negligible impact on the structural integrity of the carbon matrix. The surface chemical composition and elemental states of the as-prepared samples were investigated by X-ray photoelectron spectroscopy (XPS). The corresponding N 1s spectra (Fig. S14) exhibit three prominent peaks at 398.38, 400.08, and 401.68 eV, which are attributed to pyridinic N, pyrrolic N, and graphitic N, respectively.[50,51] In the F 1s spectra of both FCNT and Fe_{SACS}-FCNT samples, a peak corresponding to C–F bonds is clearly observed. Notably, an additional peak assigned to Fe–F bonds is identified in the Fe_{SACS}-FCNT sample,[43,52] providing direct evidence for the effective coordination between F atoms and the central Fe active sites (Fig. S15). The electronic structure evolution of Fe centers in Fe_{SACS}-FCNT and Fe_{SACS}-CNT was systematically investigated through X-ray absorption near-edge structure (XANES) spectroscopy. As illustrated in Fig. 3a, the normalized absorption

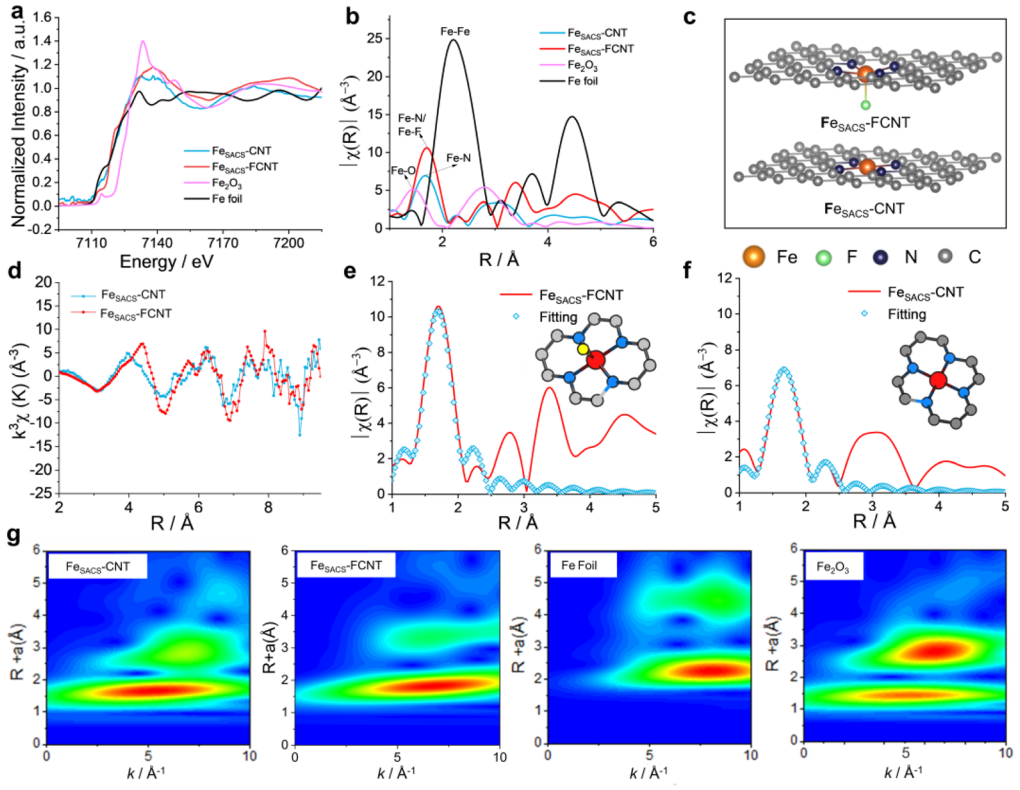

Fig. 3 (a) XANES spectra and (b) corresponding FT-EXAFS results in *R* space of Fe_{SACS}-FCNT, Fe_{SACS}-CNT, Fe foil, and Fe_2O_3. (c) Two forms of alien atom-doped single-atom structures. (d) EXAFS oscillations of Fe_{SACS}-FCNT and Fe_{SACS}-CNT. Fitting results of (e) Fe_{SACS}-FCNT and (f) Fe_{SACS}-CNT in *R* space. (g) WT analysis of Fe_{SACS}-CNT, Fe_{SACS}-FCNT, Fe foil, and Fe_2O_3.

edges of Fe_{SACS}-FCNT and Fe_{SACS}-CNT are positioned between metallic Fe foil and Fe_2O_3, indicative of partially Fe species with intermediate valence states (0 to +3). Notably, a distinct positive shift in the absorption edge energy is observed for Fe_{SACS}-FCNT relative to Fe_{SACS}-CNT, evidencing the elevated oxidation state of Fe induced by the axial Fe–F coordination.[53,54] Fig. 3b illustrates the results of the Fourier-transformed extended X-ray absorption fine structure (FT-EXAFS) analysis of Fe_{SACS}-FCNT, Fe_{SACS}-CNT and their selected standard samples. In both materials, the main peak appears at ~1.5 Å, which is attributed to the Fe–N scattering path. No Fe–Fe bonding peak is observed at ~2.2 Å,[55] demonstrating that the Fe species exist in an atomically dispersed form (Fig. 3c).

To further verify the presence of Fe–F axial coordination, FT-EXAFS curves were fitted for both sets of samples. The best fit for Fe_{SACS}-FCNT showed the coexistence of Fe–N and Fe–F bonds, with the calculated actual N and F coordination numbers of 4.48 and 0.68 (Fig. 3d, e and Table S2), respectively, suggesting that the coordination configuration consists of [56,57] four in-plane nitrogen atoms and one F atom in the axial direction. In contrast, the control sample Fe_{SACS}-CNT contains only isolated FeN_4 sites (Fig. 3f and Table S3).

To resolve the subtle differences in bonding configurations, wavelet transform (WT) analysis was employed for its superior resolution in both *k*-space and *R*-space (Fig. 3g).[58,59] The WT profiles of both Fe_{SACS}-FCNT and Fe_{SACS}-CNT at about 5.0 $Å^{-1}$ (*k*-space) and 1.5 Å (*R*-space) show one of the strongest peaks, which is attributed to the Fe–N and Fe–N/F coordination. Meanwhile, the peak of Fe_{SACS}-FCNT shifts to higher *k*-space and *R*-space, which is attributed to the stronger backscattering effect of the F ligand. This phenomenon provides direct spectral evidence for the successful construction of Fe–F axial bonds, which synergistically optimize the charge transfer kinetics and electronic polarization of Fe centers. Such precisely engineered coordination environments establish a fundamental structure–activity relationship for sulfur redox electrocatalysis in RT Na–S batteries. To systematically evaluate the electrochemical performance of Fe_{SACS}-FCNT-based and Fe_{SACS}-CNT-based sulfur cathodes, coin cells were assembled and tested within a voltage window of 0.8–2.8 V. The cyclic voltammetry (CV) test at 0.1 mV s^{-1} was employed to investigate the sulfur redox behavior. As shown in Fig. 4a, two distinct cathodic peaks during the discharge process correspond to the stepwise reduction pathway of S_8 → soluble polysulfides (Na_2S_x, $4 \leq x \leq$

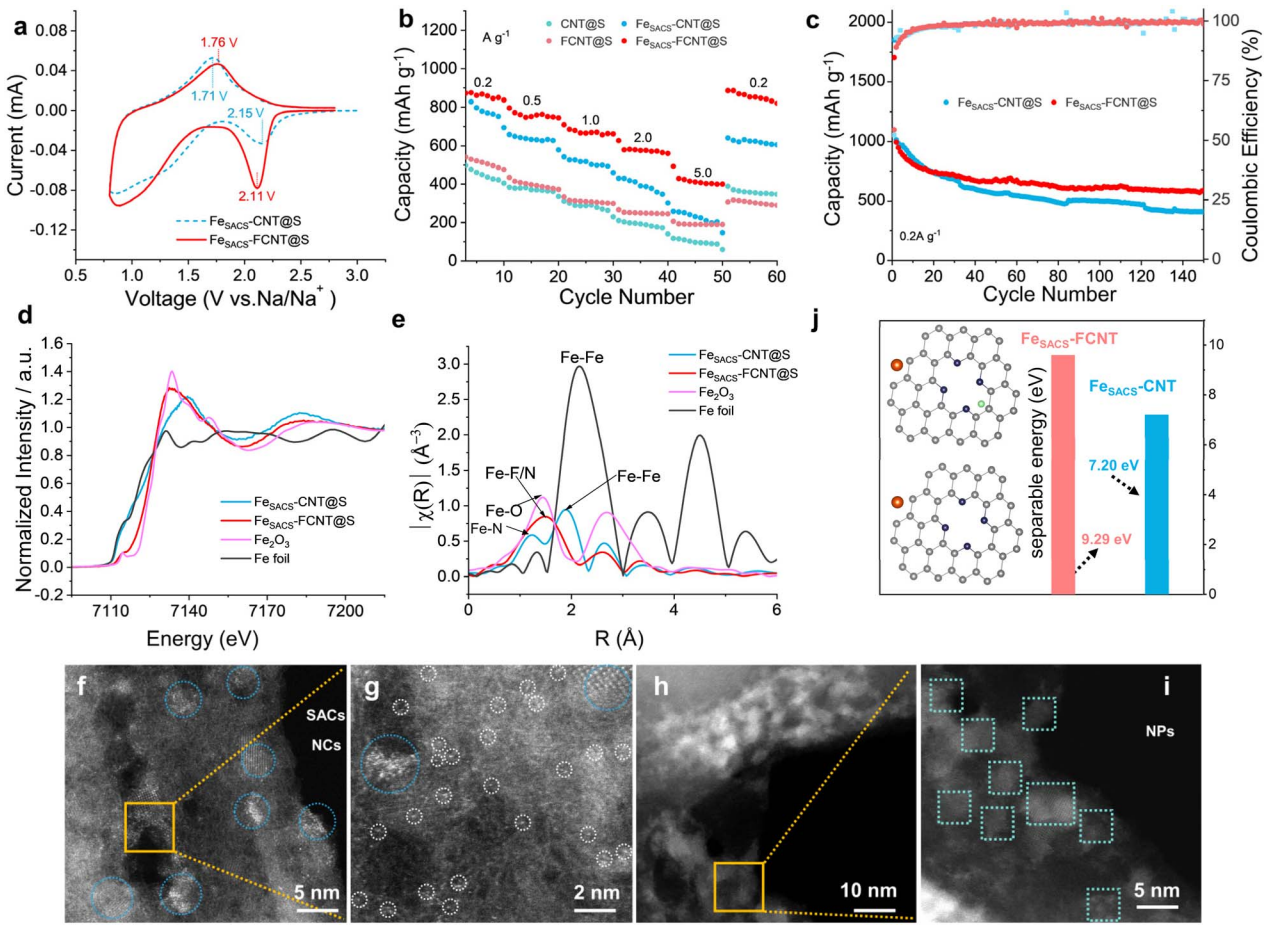

Fig. 4 (a) CV curves of the Fe_{SACS}-FCNT@S and Fe_{SACS}-CNT@S cathodes measured at 0.1 mV s^{-1}. (b) Rate capability at 0.2, 0.5, 1.0, 2.0, and 5.0 A g^{-1}, respectively. (c) Cycling performance at 0.2 A g^{-1}. (d and e) XANES spectra and corresponding FT-EXAFS results in *R* space of Fe_{SACS}-FCNT@S, Fe_{SACS}-CNT@S, Fe foil, and Fe_2O_3 after 150 cycles at 0.2 A g^{-1}. (f and g) HAADF-STEM images of Fe_{SACS}-FCNT@S and (h and i) Fe_{SACS}-CNT@S after 150 cycles at 0.2 A g^{-1}. (j) Separation energies of FeN_4 sites in Fe_{SACS}-FCNT and Fe_{SACS}-CNT.

8) → solid Na_2S_2/Na_2S, while the single anodic peak during charge arises from the reverse oxidation of Na_2S to polysulfides.[60,61] Remarkably, the Fe_{SACS}-FCNT@S electrode exhibits enhanced cathodic peak current and reduced polarization voltage, suggesting faster redox reaction kinetics.

Fig. 4b shows the rate performances of the electrodes at different current densities from 0.2 A g^{-1} to 5.0 A g^{-1}. Compared to the control group without Fe_{SACS}, both Fe_{SACS}-FCNT@S and Fe_{SACS}-CNT@S exhibit significantly enhanced initial capacity, verifying the superior performance of Fe_{SACS} in catalyzing the conversion of NaPSs. More notably, under the same test conditions, the cells based on the Fe_{SACS}-FCNT@S structure exhibited higher specific discharge capacity compared to other control groups. Even when reverting back to the current density of 0.2 A g^{-1} after high-rate cycling, a reversible capacity of up to 832.60 mA h g^{-1} is still maintained, showing excellent structural stability and cycling durability. The long-term cycling stability of Fe_{SACS}-FCNT@S and Fe_{SACS}-CNT@S was systematically evaluated (Fig. 4c and S16–S18). Remarkably, Fe_{SACS}-FCNT@S exhibited superior performance at both 0.2 A g^{-1} and 1 A g^{-1}, at a current density of 0.2 A g^{-1}, and the capacity of Fe_{SACS}-FCNT@S is still maintained at 589.5 mA h g^{-1} after 150 cycles, while that of Fe_{SACS}-CNT@S is only 409.4 mA h g^{-1}. In addition, at a high current density of 1.0 A g^{-1}, Fe_{SACS}-FCNT@S retained a capacity of 319.3 mA h g^{-1} after 1600 cycles, which is much higher than that of the control group (115.3 mA h g^{-1}). These results demonstrate that the FeN_4 sites with axial F-coordination can enhance the kinetics of the SRR. Subsequently, the GITT-derived Na^+ diffusion coefficient (D_{Na^+}) tests were carried out to investigate the reaction kinetics of Fe_{SACS}-FCNT@S and Fe_{SACS}-CNT@S. It is noteworthy that D_{Na^+} confirmed (Fig. S19) that Fe_{SACS}-FCNT@S achieved a D_{Na^+} value higher than that of Fe_{SACS}-CNT@S, confirming faster Na^+ diffusion kinetics, which contributes to the improvement of the overall electrochemical performance. Furthermore, *in situ* electrochemical impedance spectroscopy (EIS) was employed to reveal the kinetic nature of Fe_{SACS}-FCNT@S and Fe_{SACS}-CNT@S during the SRR, and the *in situ* characterization was performed in the first discharge/charge cycle. Typically, the EIS curve consists of three components: the electrolyte internal resistance (R_o), the interface resistance (R_s) and the Warburg impedance (R_o).[62] As shown in Fig. S20, at the beginning of the discharge process, the R_o of both groups of samples slightly increased, which may be related to the change of electrolyte viscosity due to the dissolution of a small amount of NaPSs. With the increase of discharge depth, R_o decreased due to the gradual conversion of soluble NaPSs into insoluble Na_2S. During the charging process, the above changes are basically reversible. Notably, Fe_{SACS}-FCNT@S consistently exhibited smaller R_o and R_s throughout the charging and discharging cycles, suggesting that its electrodes have faster charge transfer rate and more efficient electron transfer capability. Combined with the aforementioned characterization results, it further confirms that Fe_{SACS}-FCNT@S possesses excellent kinetic performance in the sulfur conversion process. In addition, the *ex situ* EIS was conducted on the four sample groups (CNT@S, FCNT@S, Fe_{SACS}-CNT@S, and Fe_{SACS}-FCNT@S). As shown in Fig. S21, the results clearly demonstrate that Fe_{SACS}-CNT@S and Fe_{SACS}-FCNT@S electrodes exhibit superior electronic conductivity and enhanced charge transfer kinetics, attributable to the presence of Fe-based single-atom catalysts. The effect of F-axial coordination on the structural properties of the material itself has been confirmed earlier by a series of characterization studies. However, under operating conditions, metal atoms may detach from the carbon support due to chemical reactions during the catalysis process and form severe aggregates, leading to a loss of catalytic activity. Therefore, we further analyze the effect of F-axial coordination on the stabilization of single-atom systems. First, we performed the XANES test on two sets of samples after 150 cycles to check the morphological evolution of Fe_{SACS}. As shown in Fig. 4d, the valence of Fe in Fe_{SACS}-FCNT@S remained between 0 and +3, indicating the existence of mainly atomic Fe species with good structural stability. In contrast, the valence of Fe in Fe_{SACS}-CNT@S tends to approach the 0-valence of Fe metal particles. Furthermore, FT-EXAFS analyses and WT transform (Fig. 4e and S22) analysis reveal differences in the coordination environments of the two samples after cycling: the first shell coordination of Fe in Fe_{SACS}-CNT@S is cleaved into two peaks and a peak belonging to the Fe–Fe bond is observed at ~2.2 Å,[47] indicating degradation of the Fe central structure and irreversible metal leaching. In contrast, Fe in Fe_{SACS}-FCNT@S maintained similar coordination interactions to the initial state throughout the cycling process, with only minor changes observed in the oxidation state and coordination environment of the FeN_4 center and thus was able to significantly retain its catalytic activity throughout the cycling process, which is also consistent with its excellent electrochemical performance. Post-cycle TEM and HAADF-STEM characterization of the two electrodes further corroborated the above findings. As shown in the TEM images (Fig. S23), no Fe nanoparticles were discerned in Fe_{SACS}-FCNT@S, whereas they were clearly observable in Fe_{SACS}-CNT@S. HAADF-STEM analysis provided further visual evidence as displayed in Fig. 4f and g, and the majority of Fe single atoms in Fe_{SACS}-FCNT@S remained atomically dispersed without significant agglomeration. In contrast, pronounced aggregation of Fe species occurred in Fe_{SACS}-CNT@S, leading to the formation of large metal clusters and particles (Fig. 4h and i).

In order to further understand the potential demetallization trend of FeN_4 active sites in RT Na–S cells, we performed DFT calculations. We evaluated the energy required to detach the metal atoms from the carbon matrix, as shown in Fig. 4j. In the Fe_{SACS}-FCNT structure, Fe atoms require a higher detachment energy to escape from the carbon matrix, suggesting that F doping significantly enhances the anchoring stability of the Fe single atom centers. In addition, we calculated the –pCOHP to evaluate the bonding strength between the metal atoms and their coordination ligands. The –pCOHP values for the Fe–N and Fe–F bonds are −2.54 eV and −2.80 eV, respectively (Fig. S24), which suggests that the additional axial coordination of Fe–F in the Fe_{SACS}-FCNT system has stronger bonding interactions than pure FeN_4 planar coordination bonding, and thus Fe single-atom leaching during synthesis and cycling is less likely. These calculations are in good agreement with our

experimental observations and provide strong support for the role of F axial coordination in enhancing the stability of FeN_4 active sites. The dissolution of NaPSs is widely recognized as a critical factor leading to the capacity degradation of RT Na–S batteries.[7,63] In order to elucidate the mechanism by which FeN_4-catalysts promote the multistep conversion of NaPSs, we assessed the dissolution behavior of S species by qualitative measurements. We conducted spectroscopic studies to assess the reactivity between Na_2S_6 and various substrates (CNT, FCNT, Fe_{SACS}-CNT and Fe_{SACS}-FCNT). As shown in the inset of Fig. 5a, after immersing four different substrates into Na_2S_6 solution for 4 h, the two groups of Fe_{SACS}-loaded samples faded away from the yellow color to a much greater extent compared to the two groups of pure carbon tube samples, and the solution was almost completely transparent, which indicated their strong adsorption capacity for Na_2S_6, which was further confirmed from UV-Vis absorption spectra. As shown in Fig. 5b and S25, we calculated the adsorption energies of the two Fe-based catalysts for different intermediates to assess their ability to stabilize sulphur species.[17] Although Fe_{SACS}-CNT exhibits stronger adsorption towards NaPSs, this strong binding hinders S–S bond cleavage and product desorption, thereby slowing down the subsequent reduction steps[64,65]—particularly during the $Na_2S_4 \rightarrow Na_2S_2$ transformation, which is the rate-determining step of the overall reaction. In contrast, Fe_{SACS}-FCNT shows a moderate interaction with intermediates, enabling faster sulfur conversion and highlighting the crucial balance between atomic utilization and sulfur redox efficiency.

In order to gain a deeper understanding of the evolutionary behavior of sulfur species during the reaction process on the surface of the two catalysts, we also carried out operational sulfur K-edge XAS characterization.[66,67] As shown in Fig. 5c, for the Fe_{SACS}-CNT@S electrodes, only the characteristic peak of element S_8 (2472.7 eV) was observed in the initial state, and this signal can still be detected at different reaction stages, suggesting that part of the sulfur exists in the form of irreversible deposition, which fails to participate in the reaction effectively. The typical characteristic peak (2468.2 eV) corresponding to NaPSs appeared at the beginning of the discharge, which gradually weakened as the discharge continued, and the characteristic absorption of Na_2S appeared at 0.8 V, indicating that the soluble polysulfides were gradually converted to insoluble Na_2S. In the two charging states (1.6 V and 2.8 V) the conversion of $Na_2S \rightarrow$ NaPSs $\rightarrow S_8$ through a reversible transformation process was also verified. Similarly, identical tests were conducted on Fe_{SACS}-FCNT@S (Fig. 5d) samples at the same voltage, revealing only the characteristic peaks of S8 and the final product Na_2S.[17,47] Upon charging back to 2.8 V, the photon energy of S_8 intensified, indicating its recovery. This observation confirms the reduction of sulfur and the gradual breaking of S–S bonds, demonstrating a highly reversible process. This reversibility was further validated by S 2p XPS test analysis (Fig. S26). These findings suggest that both electrodes undergo reversible transformations from S8 to various sulfides, reaffirming the feasibility of enhancing the SRR with Fe single atoms. Time-of-flight secondary ion mass spectrometry (TOF-SIMS) further verified the spatial domain-limiting effect of the FeN_4-based sulfur anode on sulfur species during cycling. The depth analysis by TOF-SIMS elucidated the spatial distribution of the NaPS components. As shown in Fig. 5e, the signal

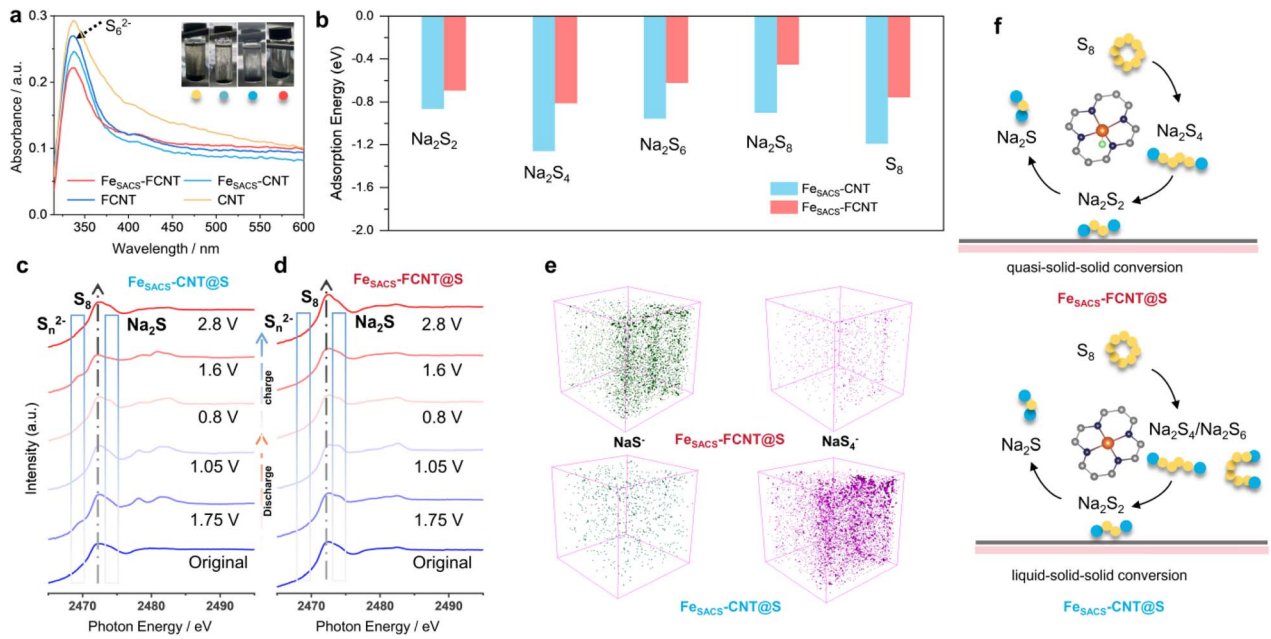

Fig. 5 (a) UV-vis absorption spectra (inset: the optical image of visualized adsorption of Na_2S_6 on CNT, FCNT, Fe_{SACS}-CNT and Fe_{SACS}-FCNT). (b) Optimized configuration of adsorbed NaPSs on the surface of Fe_{SACS}-CNT and Fe_{SACS}-FCNT. *Ex situ* sulfur K-edge analysis of the Fe_{SACS}-CNT@S (c) and Fe_{SACS}-FCNT@S (d) electrodes at different discharged states (original, 1.75, 1.05, and 0.8 V) and charged states (1.6, and 2.8 V). (e) TOF-SIMS 3D rendering NaS^- and NaS_4^- depth profile image of Fe_{SACS}-FCNT@S (up) and Fe_{SACS}-CNT@S (down). (f) Schematic of Fe_{SACS}-FCNT and Fe_{SACS}-CNT in a RT Na–S battery.

intensity of NaS_4^- at the Fe_{SACS}-CNT@S electrode was significantly stronger than that of Fe_{SACS}-FCNT@S samples after 150 cycles at a small current density of 0.2 A g^{-1}, and furthermore, the content of NaS^- was more distributed in the Fe_{SACS}-FCNT@S electrode. This verified that the Fe_{SACS}-CNT@S samples presented higher NaPS aggregation concentration, both indicating that the Fe_{SACS}-FCNT@S system had a stronger ability to catalyze the transformation of polysulfides. In conjunction with the above tests, it was found that no long-chain intermediate sulfur species were detected in the Fe_{SACS}-FCNT@S system due to the relatively moderate adsorption strength of these intermediates (Fig. 5c), which are rapidly converted to the next intermediate up to Na_2S_2, and thus are not readily detected in the *ex situ* tests. This further highlights the increased conversion efficiency of NaPSs through F-axis coordination. This interaction transformed the redox pathway from the traditional liquid–solid–solid conversion to a more efficient quasi-solid–solid conversion, thus effectively suppressing the shuttle effect within the electrolyte.[68–70] Fig. 5f schematically illustrates the different reaction pathways for Fe_{SACS}-CNT@S and Fe_{SACS}-FCNT@S. The conventional sulfur transformation pathway can be represented as $S_8 \leftrightarrow Na_2S_{8/6} \leftrightarrow Na_2S_4 \leftrightarrow Na_2S_2/Na_2S$. For the Fe_{SACS}-CNT@S cathode, the introduction of FeN_4 catalytic sites promotes the rapid conversion of polysulfides to Na_2S, forming a fast liquid–solid–solid reaction pathway. Further optimization of the sulfur formation pathway is achieved through axial F coordination, which refines the local environment around Fe single atoms, enabling a quasi-solid–solid reaction route. This leads to significantly improved suppression of polysulfide shuttling and markedly enhanced sulfur utilization efficiency.

Conclusions

In summary, a new strategy based on fluorine ligands to modulate the coordination environment of the second shell layer is proposed using FeN_4-type single-atom catalysts as a model system, aiming at solving key problems such as the slow kinetics of the SRR and the serious shuttle effect of NaPSs in RT Na–S batteries. The local electronic structure of the Fe active centre is precisely modulated by F doping, and DFT calculations show that the strategy effectively modulates the 3d orbital distribution of Fe and enhances its d–p orbital interactions with NaPSs, which significantly improves the adsorption and conversion kinetics of NaPSs. The experimental results further validate the dual advantages of this modification strategy in enhancing the intrinsic activity and structural stability in the FeN_4 single-atom system. In short, Fe_{SACS}-FCNT@S exhibits superior performance and cycling stability compared with the conventional Fe_{SACS}-CNT@S battery system. In addition, Fe_{SACS}-FCNT@S shows that the iron species remain atomically dispersed after 150 cycles, whereas Fe_{SACS}-CNT@S shows obvious metal agglomeration. In addition, we have also combined various characterization studies to systematically reveal the dynamic evolution of sulfur species during the charging and discharging process, identified two different reaction pathways, and established a conformational relationship between 'coordination environment–electronic structure–catalytic activity'.

Author contributions

All authors have given approval to the final version of the manuscript.

Conflicts of interest

There are no conflicts to declare

Data availability

The data that support the findings of this study are available from the corresponding author upon reasonable request.

Supplementary information: Experimental procedures and additional characterization details, DFT calculations, SEM, TEM, XRD, BET, Raman analysis, XPS, discharge/charge profiles, GITT, EIS, WT analysis and tables. See DOI: **https://doi.org/10.1039/d5sc05972k**.

Acknowledgements

This work was financially supported by the National Natural Science Foundation of China (22379165, 52074359, U21A20284, and U22B2069) supported by the Fundamental Research Funds for the Central Universities of Central South University (2024ZZTS0389).

Notes and references

1 L. Zhao, Y. Tao, Y. Zhang, Y. Lei, W. H. Lai, S. Chou, H. K. Liu, S. X. Dou and Y. X. Wang, A Critical Review on Room-Temperature Sodium-Sulfur Batteries: From Research Advances to Practical Perspectives, *Adv. Mater.*, 2024, **36**, e2402337.
2 M. K. Aslam, I. D. Seymour, N. Katyal, S. Li, T. Yang, S. J. Bao, G. Henkelman and M. Xu, Metal chalcogenide hollow polar bipyramid prisms as efficient sulfur hosts for Na-S batteries, *Nat. Commun.*, 2020, **11**, 5242.
3 N. Hong, S. Zhang, J. Li, H. Wang, J. Huang, X. Hu, B. Zhang, F. Hua, J. Zeng, W. Jian, C. Sun, N. Bugday, W. Deng, G. Zou, H. Hou, Z. Hu, Z. Long, Y. Wu and X. Ji, Full-Scale Regulation Enabled High-Performance Sodium O3-Type Layered Cathodes, *Angew Chem. Int. Ed. Engl.*, 2025, **64**, e202423479.
4 Y. Gao, X. Chen, X. Jin, C. Zhang, X. Zhang, X. Liu, Y. Li, Y. Li, J. Lin, H. Gao and G. Wang, Multifunction integration within magnetic CNT-bridged MXene/CoNi based phase change materials, *eScience*, 2024, **4**, 100292.
5 X. L. Huang, Y.-X. Wang, S.-L. Chou, S. X. Dou and Z. M. Wang, Materials engineering for adsorption and catalysis in room-temperature Na–S batteries, *Energy Environ. Sci.*, 2021, **14**, 3757–3795.
6 W. Yao, M. H. Pai and A. Manthiram, Deciphering the Impact of Polysulfide Solvation Structure on Electrical

Double Layer Chemistry in Sodium-Sulfur Batteries, *Angew Chem. Int. Ed. Engl.*, 2025, **64**, e202424547.

7 Y. Yuan, Y. Hu, Y. Gan, Z. Dong, Y. Wang, E. Jin, M. Yang, F. B. Holness, V. Martins, Q. Tu and Y. Zhao, Self-sacrifice of sulfide electrolytes facilitating stable solid-state sodium–sulfur batteries, *Energy Environ. Sci.*, 2025, **18**, 4288–4301.

8 Y. J. Lei, X. X. Lu, H. Yoshikawa, D. Matsumura, Y. M. Fan, L. F. Zhao, J. Li, S. Wang, Q. F. Gu, H. K. Liu, S. X. Dou, S. Devaraj, T. Rojo, W. H. Lai, M. Armand, Y. X. Wang and G. X. Wang, Understanding the charge transfer effects of single atoms for boosting the performance of Na-S batteries, *Nat. Commun.*, 2024, **15**, 3325.

9 J. R. Mou, Y. J. Li, T. Liu, W. J. Zhang, M. Li, Y. T. Xu, L. Zhong, W. H. Pan, C. H. Yang, J. L. Huang and M. L. Liu, Metal-Organic Frameworks-Derived Nitrogen-Doped Porous Carbon Nanocubes with Embedded Co Nanoparticles as Efficient Sulfur Immobilizers for Room Temperature Sodium-Sulfur Batteries, *Small Methods*, 2021, **5**, 2100455.

10 W. Hua, T. Shang, H. Li, Y. Sun, Y. Guo, J. Xia, C. Geng, Z. Hu, L. Peng, Z. Han, C. Zhang, W. Lv and Y. Wan, Optimizing the p charge of S in p-block metal sulfides for sulfur reduction electrocatalysis, *Nat. Catal.*, 2023, **6**, 174–184.

11 B. Wang, L. Wang, B. Guo, Y. Kong, F. Wang, Z. Jing, G. Qu, M. Mamoor, D. Wang, X. He, L. Kong and L. Xu, In Situ Electrochemical Evolution of Amorphous Metallic Borides Enabling Long Cycling Room-/Subzero-Temperature Sodium-Sulfur Batteries, *Adv. Mater.*, 2024, **36**, e2411725.

12 Y. Jiang, Z. Yu, X. Zhou, X. Cheng, H. Huang, F. Liu, Y. Yang, S. He, H. Pan, H. Yang, Y. Yao, X. Rui and Y. Yu, Single-Atom Vanadium Catalyst Boosting Reaction Kinetics of Polysulfides in Na-S Batteries, *Adv. Mater.*, 2023, **35**, e2208873.

13 J. Shen, J. Chen, Y. Qian, X. Wang, D. Wang, H. Pan and Y. Wang, Atomic Engineering of Single-Atom Nanozymes for Biomedical Applications, *Adv. Mater.*, 2024, **36**, e2313406.

14 K. Kong, H. Zhang, A. Han, F. Li and D. Wang, Atomically dispersed metal cocatalysts for solar energy conversion, *Energy Environ. Sci.*, 2024, **17**, 7649–7680.

15 S. Wei, M. Sun, J. Huang, Z. Chen, X. Wang, L. Gao and J. Zhang, Axial Chlorination Engineering of Single-Atom Nanozyme: Fe-N(4)Cl Catalytic Sites for Efficient Peroxidase-Mimicking, *J. Am. Chem. Soc.*, 2024, **146**, 33239–33248.

16 G. Wu, T. Liu, Z. Lao, Y. Cheng, T. Wang, J. Mao, H. Zhang, E. Liu, C. Shi, G. Zhou, C. He, W. Hu, N. Zhao, N. Wu and B. Chen, Optimizing s-p Orbital Overlap Between Sodium Polysulfides and Single-Atom Indium Catalyst for Efficient Sulfur Redox Reaction, *Angew Chem. Int. Ed. Engl.*, 2025, **64**, e202422208.

17 W. Song, Z. Wen, X. Wang, K. Qian, T. Zhang, H. Wang, J. Ding and W. Hu, Unsaturation degree of Fe single atom site manipulates polysulfide behavior in sodium-sulfur batteries, *Nat. Commun.*, 2025, **16**, 2795.

18 C. Ye, H. Jin, J. Shan, Y. Jiao, H. Li, Q. Gu, K. Davey, H. Wang and S. Z. Qiao, A Mo(5)N(6) electrocatalyst for efficient Na(2)S electrodeposition in room-temperature sodium-sulfur batteries, *Nat. Commun.*, 2021, **12**, 7195.

19 G. Yao, Z. Li, Y. Zhang, Y. Xiao, L. Wei, H. Niu, Q. Chen, Y. Yang and F. Zheng, Highly Flexible Carbon Film Implanted with Single-Atomic Zn−N_2 Moiety for Long-Life Sodium-Sulfur Batteries, *Adv. Funct. Mater.*, 2023, **34**, e2214353.

20 Y. Qiu, L. Fan, M. Wang, X. Yin, X. Wu, X. Sun, D. Tian, B. Guan, D. Tang and N. Zhang, Precise Synthesis of Fe-N(2) Sites with High Activity and Stability for Long-Life Lithium-Sulfur Batteries, *ACS Nano*, 2020, **14**, 16105–16113.

21 Y. Liu, S. Zhang, C. Jiao, H. Chen, G. Wang, W. Wu, Z. Zhuo and J. Mao, Axial Phosphate Coordination in Co Single Atoms Boosts Electrochemical Oxygen Evolution, *Adv. Sci.*, 2023, **10**, e2206107.

22 L. Yin, M. Sun, S. Zhang, Y. Huang, B. Huang and Y. Du, Chlorine Axial Coordination Activated Lanthanum Single Atoms for Efficient Oxygen Electroreduction with Maximum Utilization, *Adv. Mater.*, 2025, **37**, e2416387.

23 S. Ren, Y. Wang, L. Shi, X. Xu, S. Zhong, K. Hu, H. Zhou, Z. S. Zhu, P. Zhou, W. Tian, J. Zuo, J. Yi, X. Guan, X. Duan and S. Wang, Transforming Plastics to Single Atom Catalysts for Peroxymonosulfate Activation: Axial Chloride Coordination Intensified Electron Transfer Pathway, *Adv. Mater.*, 2025, **37**, e2415339.

24 H. Wang, T. Yang, J. Wang, Z. Zhou, Z. Pei and S. Zhao, Coordination engineering in single-site catalysts: general principles, characterizations, and recent advances, *Chem*, 2024, **10**, 48–85.

25 H. Xu, Z. Zhang, J. Liu, C. L. Do-Thanh, H. Chen, S. Xu, Q. Lin, Y. Jiao, J. Wang, Y. Wang, Y. Chen and S. Dai, Entropy-stabilized single-atom Pd catalysts via high-entropy fluorite oxide supports, *Nat. Commun.*, 2020, **11**, 3908.

26 C. Ma, Y. Zhang, Y. Feng, N. Wang, L. Zhou, C. Liang, L. Chen, Y. Lai, X. Ji, C. Yan and W. Wei, Engineering Fe-N Coordination Structures for Fast Redox Conversion in Lithium-Sulfur Batteries, *Adv. Mater.*, 2021, **33**, e2100171.

27 Q. Lv, Y. Sun, B. Li, C. Li, Q. Zhang and L. Wang, Metal–Organic Frameworks with Axial Cobalt–Oxygen Coordination Modulate Polysulfide Redox for Lithium–Sulfur Batteries, *Adv. Energy Mater.*, 2024, **15**, e2403223.

28 R. Yan, Z. Zhao, M. Cheng, Z. Yang, C. Cheng, X. Liu, B. Yin and S. Li, Origin and Acceleration of Insoluble Li(2) S(2)-Li(2) S Reduction Catalysis in Ferromagnetic Atoms-based Lithium-Sulfur Battery Cathodes, *Angew Chem. Int. Ed. Engl.*, 2023, **62**, e202215414.

29 Z. Lang, X. Wang, S. Jabeen, Y. Cheng, N. Liu, Z. Liu, T. Gan, Z. Zhuang, H. Li and D. Wang, Destabilization of Single-Atom Catalysts: Characterization, Mechanisms, and Regeneration Strategies, *Adv. Mater.*, 2025, **37**, e2418942.

30 Y. Cui, C. Ren, M. Wu, Y. Chen, Q. Li, C. Ling and J. Wang, Structure-Stability Relation of Single-Atom Catalysts under Operating Conditions of CO(2) Reduction, *J. Am. Chem. Soc.*, 2024, **146**, 29169–29176.

31 G. Bae, S. Han, H. S. Oh and C. H. Choi, Operando Stability of Single-Atom Electrocatalysts, *Angew Chem. Int. Ed. Engl.*, 2023, **62**, e202219227.

32 G. Sun, Z. J. Zhao, R. Mu, S. Zha, L. Li, S. Chen, K. Zang, J. Luo, Z. Li, S. C. Purdy, A. J. Kropf, J. T. Miller, L. Zeng and J. Gong, Breaking the scaling relationship via thermally stable Pt/Cu single atom alloys for catalytic dehydrogenation, *Nat. Commun.*, 2018, **9**, 4454.

33 A. Pedersen, K. Kumar, Y.-P. Ku, V. Martin, L. Dubau, K. T. Santos, J. Barrio, V. A. Saveleva, P. Glatzel, V. K. Paidi, X. Li, A. Hutzler, M.-M. Titirici, A. Bonnefont, S. Cherevko, I. E. L. Stephens and F. Maillard, Operando Fe dissolution in Fe–N–C electrocatalysts during acidic oxygen reduction: impact of local pH change, *Energy Environ. Sci.*, 2024, **17**, 6323–6337.

34 L. Zhang, X. Yang, Q. Yuan, Z. Wei, J. Ding, T. Chu, C. Rong, Q. Zhang, Z. Ye, F. Z. Xuan, Y. Zhai, B. Zhang and X. Yang, Elucidating the structure-stability relationship of Cu single-atom catalysts using operando surface-enhanced infrared absorption spectroscopy, *Nat. Commun.*, 2023, **14**, 8311.

35 A. Kumar, M. Gil-Sepulcre, J. P. Fandre, O. Rudiger, M. G. Kim, S. DeBeer and H. Tuysuz, Regulating Local Coordination Sphere of Ir Single Atoms at the Atomic Interface for Efficient Oxygen Evolution Reaction, *J. Am. Chem. Soc.*, 2024, **146**, 32953–32964.

36 X. Zhong, Y. Huang, J. Cai, Y. Li, Z. He, D. Cai, Z. Geng, W. Deng, G. Zou, H. Hou and X. Ji, Origin of the High Catalytic Activity of MoS(2) in Na-S Batteries: Electrochemically Reconstructed Mo Single Atoms, *J. Am. Chem. Soc.*, 2024, **146**, 32124–32134.

37 Z. Li, X. Chen, G. Yao, L. Wei, Q. Chen, Q. Luo, F. Zheng and H. Wang, Strengthening d-p Orbital-Hybridization via Coordination Number Regulation of Manganese Single-Atom Catalysts Toward Fast Kinetic and Long-Life Sodium-Sulfur Batteries, *Adv. Funct. Mater.*, 2024, **34**, e2400859.

38 L. Xiao, S. Mou, W. Dai, W. Yang, Q. Cheng, S. Liu and F. Dong, Identification of Cu(111) as Superior Active Sites for Electrocatalytic NO Reduction to NH_3 with High Single-Pass Conversion Efficiency, *Angew Chem. Int. Ed. Engl.*, 2024, **63**, e202319135.

39 F. Zheng, F. Chen, Z. Li, G. Yao, S. Dong, L. Wei, Q. Chen, C. Wang and H. Wang, Template-Sacrificing Synthesis of Asymmetrically Coordinated Zn Single-Atom Sites for High-Performance Sodium-Sulfur Batteries, *Adv. Funct. Mater.*, 2024, **35**, e2413084.

40 Z. Y. Han, S. Y. Zhao, J. W. Xiao, X. W. Zhong, J. Z. Sheng, W. Lv, Q. F. Zhang, G. M. Zhou and H. M. Cheng, Engineering Orbital Hybridization in Single-Atom Metal-Embedded Three-Dimensional Electrodes for Li-S Batteries, *Adv. Mater.*, 2021, **33**, e2405947.

41 X. Zhong, Y. J. Huang, J. M. Cai, Y. J. Li, Z. D. He, D. Y. Cai, Z. L. Geng, W. T. Deng, G. Q. Zou, H. S. Hou and X. B. Ji, Origin of the High Catalytic Activity of MoS in Na-S Batteries: Electrochemically Reconstructed Mo Single Atoms, *J. Am. Chem. Soc.*, 2024, **146**, 32124–32134.

42 C. X. Dong, C. N. Ma, C. Zhou, Y. K. Yu, J. J. Wang, K. S. Yu, C. L. Shen, J. P. Gu, K. J. Yan, A. Zheng, M. J. Gong, X. Xu and L. Q. Mai, Engineering d-p Orbital Hybridization with P, S Co-Coordination Asymmetric Configuration of Single Atoms Toward High-Rate and Long-Cycling Lithium-Sulfur Battery, *Adv. Mater.*, 2024, **36**, e2407070.

43 L. Xu, S. Li, H. Tu, F. Zhu, H. Liu, W. Deng, J. Hu, G. Zou, H. Hou and X. Ji, Molecular Engineering of Highly Fluorinated Carbon Dots: Tailoring Li(+) Dynamics and Interfacial Fluorination for Stable Solid Lithium Batteries, *ACS Nano*, 2023, **17**, 22082–22094.

44 Y. J. Lei, L. F. Zhao, W. H. Lai, Z. F. Huang, B. Sun, P. Jaumaux, K. N. Sun, Y. X. Wang and G. X. Wang, Electrochemical coupling in subnanometer pores/channels for rechargeable batteries, *Chem. Soc. Rev.*, 2024, **53**, 3829–3895.

45 W. Zhang, B. Song, M. Wang, T. Miao, X.-L. Huang, E. Zhang, X. Zhan, Y. Yang, H. Zhang and K. Lu, Confined tandem catalytic quasi-solid sulfur reversible conversion for all-solid-state Na–S batteries, *Energy Environ. Sci.*, 2024, **17**, 5273–5282.

46 B. W. Zhang, T. Sheng, Y. X. Wang, S. Chou, K. Davey, S. X. Dou and S. Z. Qiao, Long-Life Room-Temperature Sodium-Sulfur Batteries by Virtue of Transition-Metal-Nanocluster-Sulfur Interactions, *Angew Chem. Int. Ed. Engl.*, 2019, **58**, 1484–1488.

47 Y. Qi, Q. J. Li, Y. Wu, S. J. Bao, C. Li, Y. Chen, G. Wang and M. Xu, A Fe(3)N/carbon composite electrocatalyst for effective polysulfides regulation in room-temperature Na-S batteries, *Nat. Commun.*, 2021, **12**, 6347.

48 C. Wu, Y. Yang, Y. Li, X. He, Y. Zhang, W. Huang, Q. Chen, X. Liu, S. Chen, Q. Gu, L. Li, S. C. Smith, X. Tan, Y. Yu, X. Wu and S. Chou, Unraveling the structure–performance relationship in hard carbon for sodium-ion battery by coupling key structural parameters, *Energy Environ. Sci.*, 2025, **18**, 6019–6031.

49 S. Xiao, Y. J. Guo, H. X. Chen, H. Liu, Z. Q. Lei, L. B. Huang, R. X. Jin, X. C. Su, Q. Zhang and Y. G. Guo, Insight into the Role of Closed-Pore Size on Rate Capability of Hard Carbon for Fast-Charging Sodium-Ion Batteries, *Adv. Mater.*, 2025, **37**, e2501434.

50 L. Li, Y. Li, Y. Ye, R. Guo, A. Wang, G. Zou, H. Hou and X. Ji, Kilogram-Scale Synthesis and Functionalization of Carbon Dots for Superior Electrochemical Potassium Storage, *ACS Nano*, 2021, **15**, 6872–6885.

51 Y. Huang, X. Zhong, X. Hu, Y. Li, K. Wang, H. Tu, W. Deng, G. Zou, H. Hou and X. Ji, Rationally Designing Closed Pore Structure by Carbon Dots to Evoke Sodium Storage Sites of Hard Carbon in Low-Potential Region, *Adv. Funct. Mater.*, 2023, **34**, e2308329.

52 F. Zhu, L. Xu, X. Hu, M. Yang, H. Liu, C. Gan, W. Deng, G. Zou, H. Hou and X. Ji, Trace Fluorinated Carbon Dots Driven Li-Garnet Solid-State Batteries, *Angew Chem. Int. Ed. Engl.*, 2024, **63**, e202410016.

53 Y. Jiang, Z. Chen, T. Peng, L. Jiao, X. Pan, H. L. Jiang and X. Bao, Single-Atom Fe Catalysts With Improved Metal Loading for Efficient Ammonia Synthesis Under Mild

Conditions, *Angew Chem. Int. Ed. Engl.*, 2025, **64**, e202501190.

54 X. Wang, R. Zhang, X. Wu, Y. Li, Z. Wang, M. Zhao, S. Song, H. Zhang and X. Wang, Enhancing Waste Plastic Hydrogenolysis on Ru/CeO(2) Through Concurrent Incorporation of Fe Single Atoms and FeO(x) Nanoclusters, *Angew Chem. Int. Ed. Engl.*, 2025, **64**, e202506035.

55 C. Pei, G. Yao, Z. Zhao, Y. Sun, Q. Wang, T. Shang and Y. Wan, e(g) Electron Occupancy as a Descriptor for Designing Iron Single-Atom Electrocatalysts, *Adv. Mater.*, 2025, **37**, e2504852.

56 R. Lu, C. Quan, C. Zhang, Q. He, X. Liao, Z. Wang and Y. Zhao, Establishing a theoretical insight for penta-coordinated iron-nitrogen-carbon catalysts toward oxygen reaction, *Nano Res.*, 2022, **15**, 6067–6075.

57 Q. Qu, Y. Mao, S. Ji, J. Liao, J. Dong, L. Wang, Q. Wang, X. Liang, Z. Zhang, J. Yang, H. Li, Y. Zhou, Z. Wang, G. I. N. Waterhouse, D. Wang and Y. Li, Engineering the Lewis Acidity of Fe Single-Atom Sites via Atomic-Level Tuning of Spatial Coordination Configuration for Enhanced Oxygen Reduction, *J. Am. Chem. Soc.*, 2025, **147**, 6914–6924.

58 M. Xiao, Z. Xing, Z. Jin, C. Liu, J. Ge, J. Zhu, Y. Wang, X. Zhao and Z. Chen, Preferentially Engineering FeN(4) Edge Sites onto Graphitic Nanosheets for Highly Active and Durable Oxygen Electrocatalysis in Rechargeable Zn-Air Batteries, *Adv. Mater.*, 2020, **32**, e2004900.

59 S. Liu, C. Li, M. J. Zachman, Y. Zeng, H. Yu, B. Li, M. Wang, J. Braaten, J. Liu, H. M. Meyer, M. Lucero, A. J. Kropf, E. E. Alp, Q. Gong, Q. Shi, Z. Feng, H. Xu, G. Wang, D. J. Myers, J. Xie, D. A. Cullen, S. Litster and G. Wu, Atomically dispersed iron sites with a nitrogen–carbon coating as highly active and durable oxygen reduction catalysts for fuel cells, *Nat. Energy*, 2022, **7**, 652–663.

60 Y. Wang, Y. Wang, C. Xu, Y. Meng, P. Liu, C. Huang, L. Yang, R. Li, S. Tang, J. Zeng and X. Wang, Phosphor-Doped Carbon Network Electrocatalyst Enables Accelerated Redox Kinetics of Polysulfides for Sodium-Sulfur Batteries, *ACS Nano*, 2024, **18**, 3839–3849.

61 J. Ruan, Y. J. Lei, Y. Fan, M. C. Borras, Z. Luo, Z. Yan, B. Johannessen, Q. Gu, K. Konstantinov, W. K. Pang, W. Sun, J. Z. Wang, H. K. Liu, W. H. Lai, Y. X. Wang and S. X. Dou, Linearly Interlinked Fe-N(x)-Fe Single Atoms Catalyze High-Rate Sodium-Sulfur Batteries, *Adv. Mater.*, 2024, **36**, e2312207.

62 W. J. Kong, C. Z. Zhao, L. Shen, S. Sun, X. Y. Huang, P. Xu, Y. Lu, W. Z. Huang, J. L. Li, J. Q. Huang and Q. Zhang, Bulk/Interfacial Structure Design of Li-Rich Mn-Based Cathodes for All-Solid-State Lithium Batteries, *J. Am. Chem. Soc.*, 2024, **146**, 28190–28200.

63 H. Song, K. Munch, X. Liu, K. Shen, R. Zhang, T. Weintraut, Y. Yusim, D. Jiang, X. Hong, J. Meng, Y. Liu, M. He, Y. Li, P. Henkel, T. Brezesinski, J. Janek and Q. Pang, All-solid-state Li-S batteries with fast solid-solid sulfur reaction, *Nature*, 2025, **637**, 846–853.

64 H. Wang, H. Yuan, W. Wang, X. Wang, J. Sun, J. Yang, X. Liu, Q. Zhao, T. Wang, N. Wen, Y. Gao, K. Song, D. Chen, S. Wang, Y. W. Zhang and J. Wang, Accelerating Sulfur Redox Kinetics by Electronic Modulation and Drifting Effects of Pre-Lithiation Electrocatalysts, *Adv. Mater.*, 2024, **36**, e2307741.

65 W. Yao, W. Zheng, J. Xu, C. Tian, K. Han, W. Sun and S. Xiao, ZnS-SnS@NC Heterostructure as Robust Lithiophilicity and Sulfiphilicity Mediator toward High-Rate and Long-Life Lithium-Sulfur Batteries, *ACS Nano*, 2021, **15**, 7114–7130.

66 X. Gao, X. Zheng, Y. Tsao, P. Zhang, X. Xiao, Y. Ye, J. Li, Y. Yang, R. Xu, Z. Bao and Y. Cui, All-Solid-State Lithium-Sulfur Batteries Enhanced by Redox Mediators, *J. Am. Chem. Soc.*, 2021, **143**, 18188–18195.

67 D. Cao, X. Sun, F. Li, S. M. Bak, T. Ji, M. Geiwitz, K. S. Burch, Y. Du, G. Yang and H. Zhu, Understanding Electrochemical Reaction Mechanisms of Sulfur in All-Solid-State Batteries through Operando and Theoretical Studies, *Angew Chem. Int. Ed. Engl.*, 2023, **62**, e202302363.

68 Q. Pang, A. Shyamsunder, B. Narayanan, C. Y. Kwok, L. A. Curtiss and L. F. Nazar, Tuning the electrolyte network structure to invoke quasi-solid state sulfur conversion and suppress lithium dendrite formation in Li–S batteries, *Nat. Energy*, 2018, **3**, 783–791.

69 C. Xing, H. Chen, S. Qian, Z. Wu, A. Nizami, X. Li, S. Zhang and C. Lai, Regulating liquid and solid-state electrolytes for solid-phase conversion in Li–S batteries, *Chem*, 2022, **8**, 1201–1230.

70 H. Zhang, M. Wang, B. Song, X. L. Huang, W. Zhang, E. Zhang, Y. Cheng and K. Lu, Quasi-Solid Sulfur Conversion for Energetic All-Solid-State Na-S Battery, *Angew Chem. Int. Ed. Engl.*, 2024, **63**, e202402274.